arXiv:1407.2972v2 [cond-mat.quant-gas] 20 Jan 2015

Supersolid with nontrivial topological spin textures in spin-orbit-coupled Bose gases

Wei Han,[1] Gediminas Juzeliūnas,[2] Wei Zhang*,[3] and Wu-Ming Liu†[1]

[1]*Beijing National Laboratory for Condensed Matter Physics, Institute of Physics, Chinese Academy of Sciences, Beijing 100190, China*
[2]*Institute of Theoretical Physics and Astronomy, Vilnius University, A. Goštauto 12, Vilnius 01108, Lithuania*
[3]*Department of Physics, Renmin University of China, Beijing 100872, China*

Supersolid is a long-sought exotic phase of matter, which is characterized by the co-existence of a diagonal long-range order of solid and an off-diagonal long-range order of superfluid. Possible candidates to realize such a phase have been previously considered, including hard-core bosons with long-range interaction and soft-core bosons. Here we demonstrate that an ultracold atomic condensate of hard-core bosons with contact interaction can establish a supersolid phase when simultaneously subjected to spin-orbit coupling and a spin-dependent periodic potential. This supersolid phase is accompanied by topologically nontrivial spin textures, and is signaled by the separation of momentum distribution peaks, which can be detected via time-of-flight measurements. We also discuss possibilities to produce and observe the supersolid phase for realistic experimental situations.

PACS numbers: 03.75.Lm, 03.75.Mn, 67.85.Hj, 67.80.K-

I. INTRODUCTION

The search for supersolid phase has a long history since 1969 [1–6], and has been recently intensified during the debate of its possible observation in ^{4}He [7–13]. From the theoretical aspect, it has been suggested that supersolid can exist in condensates of soft-core bosons [14–16] and hard-core bosons with long-range interactions [17–19]. However, the realization of supersolid in hard-core bosons with short-range interactions is usually considered unlikely [20].

Thanks to the high controllability, ultracold atomic gases provide us an excellent platform to emulate various quantum phenomena originally considered in the context of condensed matter physics [21, 22]. Recent experimental realizations of artificial spin-orbit (SO) coupling [23–29] introduce another degree of freedom for the manipulation of atomic gases, and give opportunities for the search of novel quantum states [30–38]. Theoretical investigations reveal that the interplay among the SO coupling, interatomic interaction and external potential can lead to diverse phase diagrams for Bose gases, containing the plane wave, density stripe, composite soliton, vortex lattice, as well as quantum quasicrystal [39–47]. The SO-coupled ultracold atomic gas is also opening new perspectives in the supersolid phenomena [48, 49].

In this manuscript we investigate a hard-core Bose gas interacting via a contact (zero-range) potential. The atoms experience a spin-dependent periodic potential [50, 51] and are subjected to two-dimensional (2D) SO coupling of the Rashba-Dresselhaus type $\mathcal{V}_{\rm so} = -i\hbar(\kappa_x\sigma_x\partial_x + \kappa_y\sigma_y\partial_y)$ [52]. Here, $\sigma_{x,y}$ are the Pauli matrices and $\kappa_{x,y}$ represent the corresponding SO-coupling strengths. We demonstrate that a supersolid phase characterized by the coexistence of periodic density modulation and superfluidity can be stabilized by strong SO coupling. Comparing to a continuous system affected by SO coupling discussed in Ref. [49], the supersolid phase in the present system involving a spin-dependent periodic potential is accompanied by the spontaneous generation of a lattice composed of meron pairs and antimeron pairs, hence featuring a topologically nontrivial spin configuration. With decreasing the SO-coupling strength, this supersolid phase gives way to a state consisting of alternating spin domains separated by chiral Bloch walls. Depending on the sign of SO coupling, the chirality of the Bloch walls can be either right-handed or left-handed. We also discuss the influence of asymmetric interatomic interaction and SO coupling anisotropy ($\kappa_x \neq \kappa_y$) on the properties of the supersolid phase.

II. SPIN-ORBIT-COUPLING INDUCED SUPERSOLID

We consider SO-coupled two-component Bose-Einstein condensates in a spin-dependent periodic potential. The SO coupling is of the Rashba-Dresselhaus type, which can be realized by using a periodic pulsed magnetic field [53, 54]. The spin-dependent periodic potential is usually produced by means of the counterpropagating cross-polarized laser beams [50, 51]. Simultaneous creation of SO coupling and spin-dependent periodic potential is discussed in Appendix A. The Hamiltonian reads in the Gross-Pitaevskii mean-field approximation as

$$\mathcal{H} = \int d\mathbf{r}\mathbf{\Psi}^\dagger\left(-\frac{\hbar^2\mathbf{\nabla}^2}{2m} + \mathcal{V}_{\rm so}\right)\mathbf{\Psi} + \int d\mathbf{r}\sum_{\alpha=\uparrow,\downarrow} V_\alpha\Psi_\alpha^*\Psi_\alpha + \frac{1}{2}\int d\mathbf{r}\sum_{\alpha,\beta=\uparrow,\downarrow} g_{\alpha\beta}\Psi_\alpha^*(\mathbf{r})\Psi_\beta^*(\mathbf{r})\Psi_\beta(\mathbf{r})\Psi_\alpha(\mathbf{r}), \quad (1)$$

*wzhangl@ruc.edu.cn
†wliu@iphy.ac.cn

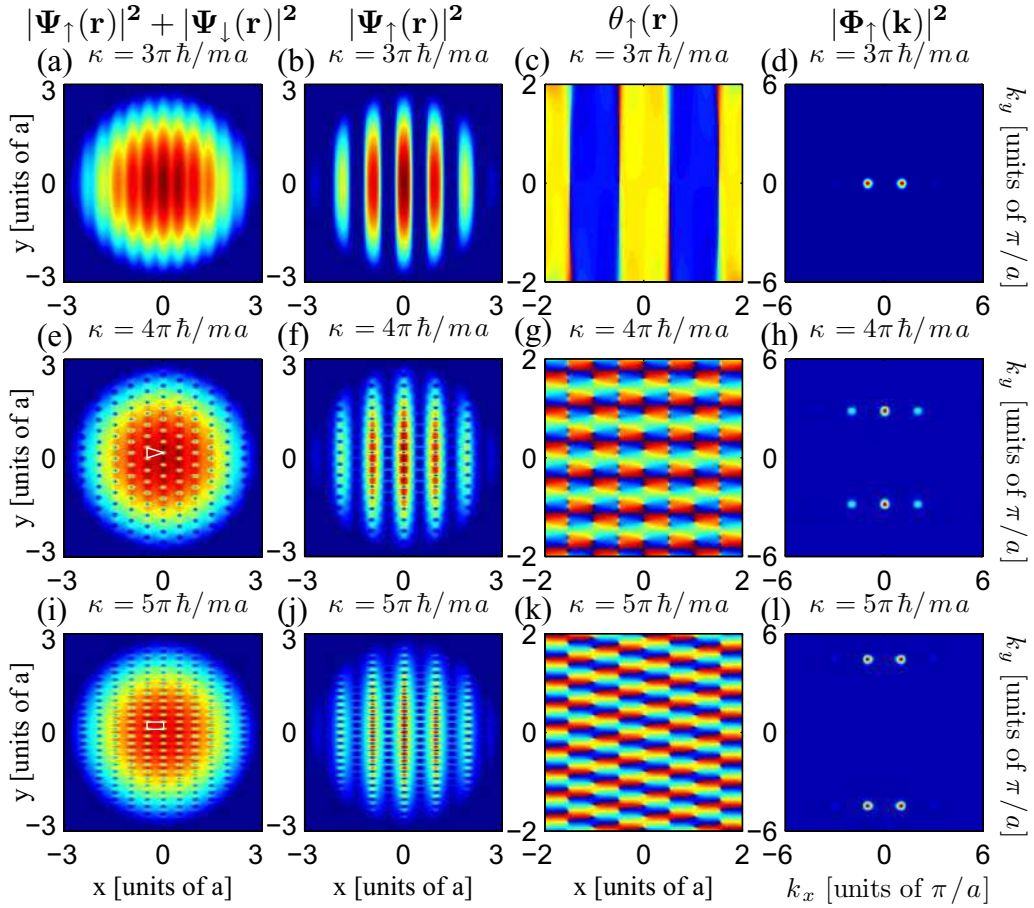

FIG. 1: (Color online) Spin-orbit-coupling induced transition from superfluid to supersolid. Various ground-state properties of Rashba SO-coupled Bose gases loaded in a 1D spin-dependent periodic potential are shown, with the SO-coupling strength $\kappa = 3\pi\hbar/ma$ (top), $4\pi\hbar/ma$ (middle), and $5\pi\hbar/ma$ (bottom). With increasing SO-coupling strength, the system undergoes a phase transition from the superfluid phase (top) to a supersolid phase (middle and bottom) characterized by density modulation along the y direction (first and second columns). The supersolid phase features a triangular lattice (middle) and a rectangular lattice (bottom) at intermediate and high SO-coupling strengths, respectively. The supersolid is accompanied by a spontaneous generation of vortex and antivortex chains in the spin-up and spin-down domains, respectively, as can be seen from the condensate phase modulation (third column). The occurrence of the supersolid phase is signaled by the separation of the momentum distribution peaks (fourth column), and can be readily observed via time-of-flight measurements. Other parameters used in these plots are $V_0 = 20\pi^2\hbar^2/ma^2$ and $\tilde{g} = 6000$.

where the complex-valued order parameter $\mathbf{\Psi} = [\Psi_\uparrow(\mathbf{r}), \Psi_\downarrow(\mathbf{r})]^\top$ is normalized to the total particle number N as $\int d\mathbf{r}\mathbf{\Psi}^\dagger\mathbf{\Psi} = N$. The strength of the atom-atom interaction $g_{\alpha\beta} = 4\pi\hbar^2 a_{\alpha\beta}/m$ is characterized by the s-wave scattering length $a_{\alpha\beta}$. The SO-coupling term can be written as $\mathcal{V}_{\rm so} = -i\hbar(\kappa_x\sigma_x\partial_x + \kappa_y\sigma_y\partial_y)$, where $\sigma_{x,y}$ are the Pauli matrices and $\kappa_{x,y}$ denote the SO-coupling strengths. In the isotropic case when $\kappa_x = \kappa_y$, the SO coupling belongs to the Rashba type. The spin-up and spin-down atoms are subjected to the spin-dependent periodic potentials $V_\uparrow = V_0\sin^2(\pi x/a)$ and $V_\downarrow = V_0\cos^2(\pi x/a)$, respectively.

The many-body ground state can be obtained by numerically minimizing the Hamiltonian functional given by Eq. (1), as outlined in Appendix B. In our calculation, we additionally introduce a weak harmonic trap $V_{\rm H} = m[\omega_\perp^2(x^2+y^2) + \omega_z^2 z^2]/2$ with $\omega_\perp = \pi^2\hbar/ma^2$ to simulate realistic configurations of cold atom experiments. When $\lambda = \omega_z/\omega_\perp \gg 1$, the condensates can be regarded as quasi-2D, and the effective interaction parameter in a 2D dimensionless form is $\tilde{g}_{\alpha\beta} = 2\sqrt{2\pi}Na_{\alpha\beta}/a_{hz}$, where $a_{hz} = \sqrt{\hbar/m\omega_z}$. Considering that the differences in $a_{\uparrow\uparrow}$, $a_{\downarrow\downarrow}$ and $a_{\uparrow\downarrow}$ are within 1% in typical experiments involving the magnetic sublevels of alkali atoms, first we focus on the case of SU(2) symmetric interactions with $\tilde{g} = \tilde{g}_{\uparrow\uparrow} = \tilde{g}_{\downarrow\downarrow} = \tilde{g}_{\uparrow\downarrow}$.

For a fixed value of atom-atom interaction, we observe a transition from the superfluid phase to a supersolid phase with increasing Rashba SO-coupling strength κ, as one can see in Fig. 1. Specifically, when the SO coupling is weak, the ground state of the system consists of alternating spin domains, where stripes filled with spin-

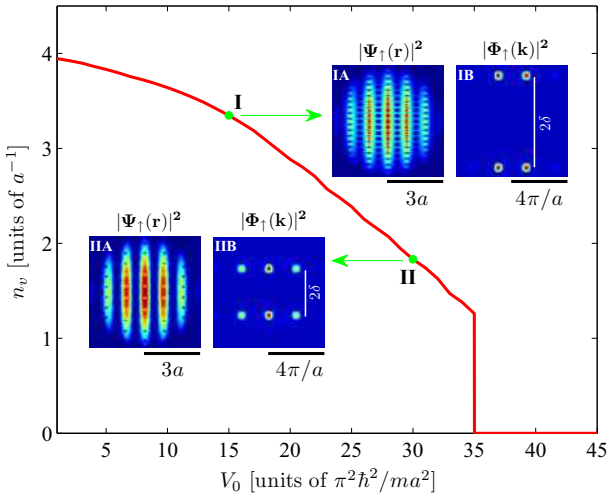

FIG. 2: (Color online) Line density of vortices as a function of periodic potential depth. With increasing the depth V_0 of the periodic potential, the line density n_v of the vortices decreases gradually, and drops to zero suddenly at the transition point $V_0 = 35\pi^2\hbar^2/ma^2$ between the supersolid and superfluid phases. The insets depict the change of vortex density and atomic momentum distributions. The line density n_v of the vortices is proportional to the separation δ of the momentum distribution peaks, and can be expressed as $n_v = \delta/\pi$. The Rashba SO-coupling strength is fixed at $\kappa = 4\pi\hbar/ma$, and the dimensionless interaction parameter is taken as $\tilde{g} = 6000$.

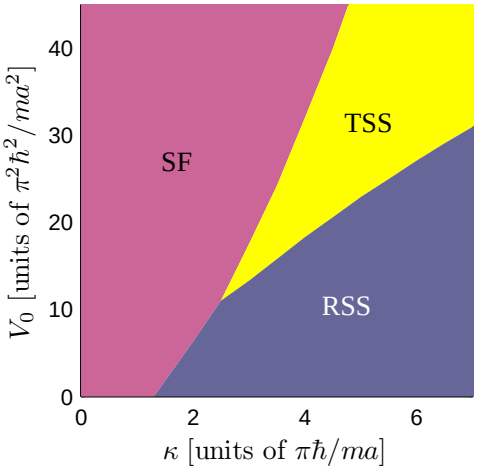

FIG. 3: (Color online) The ground-state phase diagram spanned by the Rashba SO-coupling strength κ and the periodic potential depth V_0. Three phases can be identified on this phase diagram, including the superfluid (SF) phase, the triangular supersolid (TSS) phase and the rectangular supersolid (RSS) phase. The dimensionless interaction parameter is taken as $\tilde{g} = 6000$.

up and spin-down atoms are segregated [see Figs. 1(a) and 1(b)]. While the translational symmetry along the x direction is explicitly broken by the spin-dependent periodic potential, the system preserves its translational symmetry along the y direction. If the strength of the SO coupling is increased beyond a critical value, the translational symmetry along the y direction is spontaneously broken. As a result, a new phase with periodic density modulation along the y direction is stabilized [see Figs. 1(e)-1(f) and 1(i)-1(j)], and hence can be considered as a supersolid state. The emergence of such a density modulation can be understood as a stripe phase along the y direction induced by SO coupling. However, this supersolid phase also exhibits exotic spin textures, which will be discussed below. The momentum distribution of the supersolid phase features a qualitative difference from the superfluid phase. In the superfluid phase, the atoms are condensed at a set of discrete points on the edge of Brillouin zones with finite momenta ($k_x \in K, k_y = 0$), where $K = \{\pm\pi/a, \pm 3\pi/a, \pm 5\pi/a, ...\}$ [see Fig. 1(d)]. In the supersolid phase, the momentum distribution peaks are separated from $k_y = 0$ to $k_y = \pm\delta$. The separation distance $\delta \in (0, m\kappa/\hbar)$ depends on the SO-coupling strength [see Figs. 1(h) and 1(l)] and the periodic potential depth [see Fig. 2]. This qualitative difference can be detected using conventional time-of-flight imaging technique.

In addition to the density modulation along the y direction, the supersolid phase is also characterized by a vortex lattice structure consisting of vortex and antivortex chains in the spin-up and spin-down domains, respectively [see Figs. 1(e)-1(g) and 1(i)-1(k)]. Depending on the competition between the SO-coupling strength and periodic potential depth, two different arrangements of vortices can be stabilized. In one case, the vortices of the neighboring chains are staggered, forming a triangular lattice [Fig. 1(e)]. In the other case, the vortices of the neighboring chains are parallel, forming a rectangular lattice [Fig. 1(i)]. As shown in Figs. 1(h) and 1(l), these two different vortex lattices correspond to qualitatively different momentum distributions, and hence can be distinguished by experiments. In Fig. 3, we present the ground-state phase diagram spanned by the SO-coupling strength κ and the periodic potential depth V_0, with the effective interaction parameter being $\tilde{g} = 6000$.

We stress that a vortex lattice is not directly associated with the supersolid phase, as it is absent in the supersolid droplet crystals [15]. In the present system, the generation of vortices is a direct consequence of the interplay between the SO coupling, spin-dependent periodic potential, and interatomic interactions. This is very different from the usual manner of creating supersolid vortices by rotation [16] or artificial magnetic fields [19].

The alternating arrangement of vortex and antivortex chains can be viewed as alternating plane waves propagating on opposite directions along the y axis, as shown in Figs. 1(g) and 1(k). According to the Onsager-Feynman quantization condition [55] $\oint_\mathcal{C} \mathbf{v}_\mathrm{s} \cdot d\mathbf{l} = 2\pi\hbar N_\mathrm{v}/m$, we can express the line density of the vortices as $n_\mathrm{v} = k_y/\pi$, where $k_y = \delta$ is the wave number of the plane waves. Numerical simulations show that for a given SO-coupling strength κ the line density of vortices decreases from

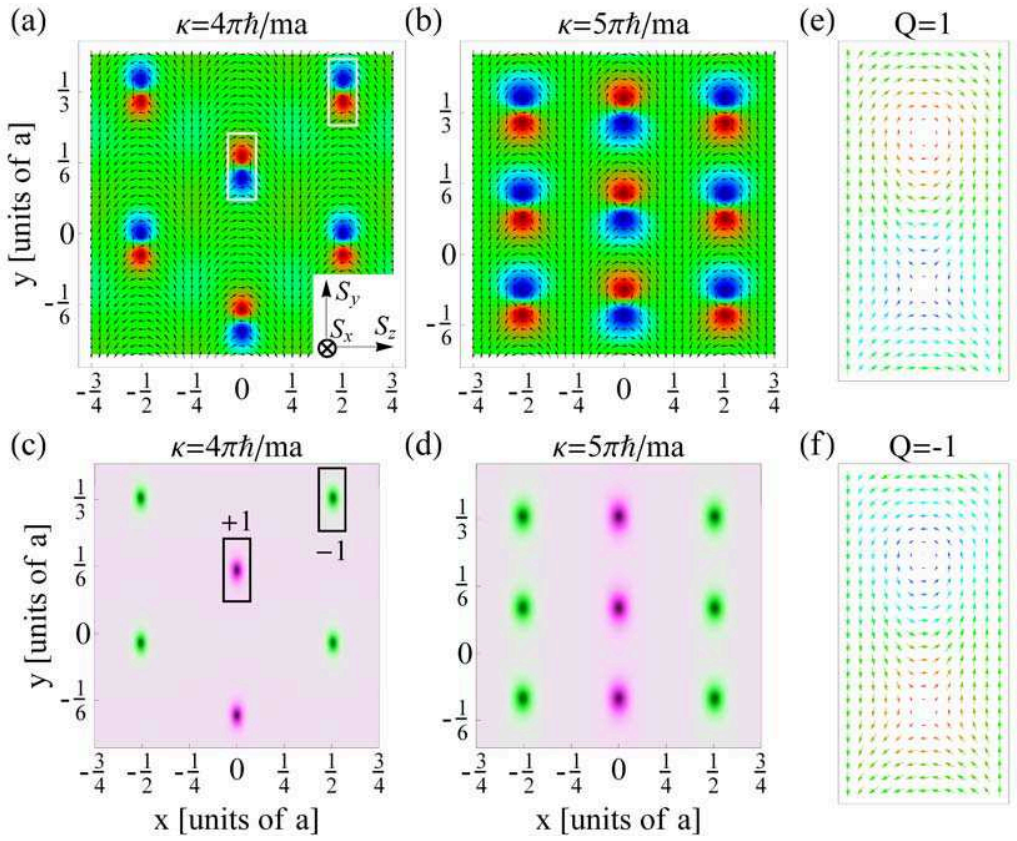

FIG. 4: (Color online) Topological spin textures. (a), (b) Spin configurations of the triangular and rectangular supersolid phases showing the spontaneous emergence of meron pairs and antimeron pairs. In these plots, the arrows represent the directions of spin vector (S_z, S_y) and the colors ranging from blue to red describe the values of S_x from -1 to 1. (c), (d) Density distributions $q(\mathbf{r})$ of topological charge for the spin textures shown in (a) and (b). The pink and green bubbles indicate that the meron pairs and antimeron pairs carry positive and negative topological charges, respectively. (e), (f) Schematic spin configurations of a meron pair (e) and an antimeron pair (f). Both the meron pairs and antimeron pairs have the same "circular-hyperbolic" structure, but with opposite spin orientations. Parameters used in these plots are identical to those used in Figs. 1(e)-1(h) and 1(i)-1(l).

$m\kappa/\pi\hbar$ to 0 with increasing the periodic potential depth V_0, as one can see in Fig. 2.

III. TOPOLOGICAL SPIN TEXTURES

The two-component Bose gas can be considered as a magnetic system. Thus one might naturally think that the supersolid transition would be associated with some magnetic ordering. We next demonstrate that the supersolid indeed features topologically nontrivial spin textures. To see this, we define a spin density vector $\mathbf{S} = \mathbf{\Psi}^\dagger \boldsymbol{\sigma} \mathbf{\Psi}/|\mathbf{\Psi}|^2$ in the pseudospin representation, where $\boldsymbol{\sigma}$ is the Pauli matrix vector. Vectorial plots of $\mathbf{S}$ (under a pseudospin rotation $\sigma_x \to \sigma_z$ and $\sigma_z \to -\sigma_x$) are shown in Figs. 4(a) and 4(b) for the triangular and rectangular lattices, respectively, where the parameters are the same as in Figs. 1(e) and 1(i). In both Figs. 4(a) and 4(b), the spin texture represents a spontaneous magnetic ordering in the form of crystals of meron pairs and antimeron pairs [56]. The meron pairs reside in the spin-up domains, while the antimeron pairs reside in the spin-down ones. We note that a meron is a topological configuration in which the spin points up or down at the meron core and rotates away from the core. Both a meron pair and an antimeron pair have a "circular-hyperbolic" structure, and the only difference is that they have exactly opposite spin orientations [see Figs. 4(e) and 4(f)].

The topological nature of the spin textures can be characterized by the topological charge Q (Chern number), which is defined as a spatial integral of the topological charge density $q(\mathbf{r}) = (1/8\pi)\epsilon^{ij}\mathbf{S}\cdot\partial_i\mathbf{S}\times\partial_j\mathbf{S}$. In Figs. 4(c) and 4(d), we present the topological charge density distribution for the triangular and rectangular lattices, respectively. Notice that both meron pairs and antimeron pairs are topologically nontrivial. A meron pair carries a topological charge 1, while an antimeron pair carries a topological charge -1. As a comparison, the topological charge density is zero everywhere in the topologically trivial superfluid phase.

Topological spin texture lattices, such as meron-pair and skyrmion lattices, are usually stabilized by bulk rotation [57–59]. Recently, it has been also suggested that skyrmion lattices can be realized by the combined effects of SO coupling and harmonic trap [43], provided that the trapping potential energy $\hbar\omega_\perp$ is higher than the characteristic interaction energy $\tilde{g}\hbar\omega_\perp$ (i.e., $\tilde{g} < 1$) [44]. Our results demonstrate that meron-pair lattices can also be stabilized by the combined effects of SO coupling and spin-dependent periodic potential, within a large regime of interatomic interaction strength. For example, the meron-pair lattices in Figs. 4(a) and 4(b) are obtained at the large effective interaction strength with $\tilde{g} = 6000 \gg 1$. This interaction strength can be naturally realized in experiments under realistic conditions without resort to the Feshbach resonance. This observation hence provides a way to create and manipulate topological spin textures in SO-coupled systems.

IV. CHIRAL DOMAIN WALLS

After discussing the novel properties of the supersolid state in the previous sections, here we investigate the superfluid phase appearing at weak SO coupling. In this phase, the translational symmetry along the y axis (orthogonal to the direction of the 1D periodic potential) is preserved, such that the system does not support density modulation along this axis. However, the presence of SO coupling breaks the spin-rotational symmetry in the S_x-S_y plane, and leads to spontaneous chiral domain walls.

In order to give a clear description of this phenomenon, we first consider the effect of SO coupling on the relative phase $\theta_\uparrow - \theta_\downarrow$ of the two component condensates, where $\theta_\uparrow$ and $\theta_\downarrow$ represent the phases of the spin-up and spin-down wave functions, respectively. In the absence of SO coupling, the Hamiltonian of Eq. (1) does not depend on the relative phase between the two spin components. In the presence of SO coupling, for the superfluid phase illustrated in Figs. 1(a)-1(d), the phase of the components does not alter except periodic jumps in the x direction [see Fig. 1(c)], thus we have $\nabla\theta_\uparrow = \nabla\theta_\downarrow = 0$. Due to the translational symmetry, the gradient of the density along the y direction can be approximately considered as $\partial_y|\Psi_\uparrow|^2 \simeq \partial_y|\Psi_\downarrow|^2 \simeq 0$, so the SO-coupling term in Eq. (1) can be represented as

$$\int \mathbf{\Psi}^\dagger \mathcal{V}_{\rm so} \mathbf{\Psi} d\mathbf{r} = 2\kappa \int |\Psi_\downarrow|\partial_x|\Psi_\uparrow| \sin(\theta_\uparrow - \theta_\downarrow) d\mathbf{r}. \quad (2)$$

One can easily see that in the presence of SO coupling, the Hamiltonian depends on the relative phase $\theta_\uparrow - \theta_\downarrow$. By minimizing the energy functional, the relative phase of the ground-state wave functions has to be locked at $\pm\pi/2$, where the sign $\pm$ is determined by the sign of $\partial_x|\Psi_\uparrow|$. As a result, the periodic density modulation along the x direction leads to a relative phase alternating between $\pi/2$ and $-\pi/2$ [see Fig. 5(a)].

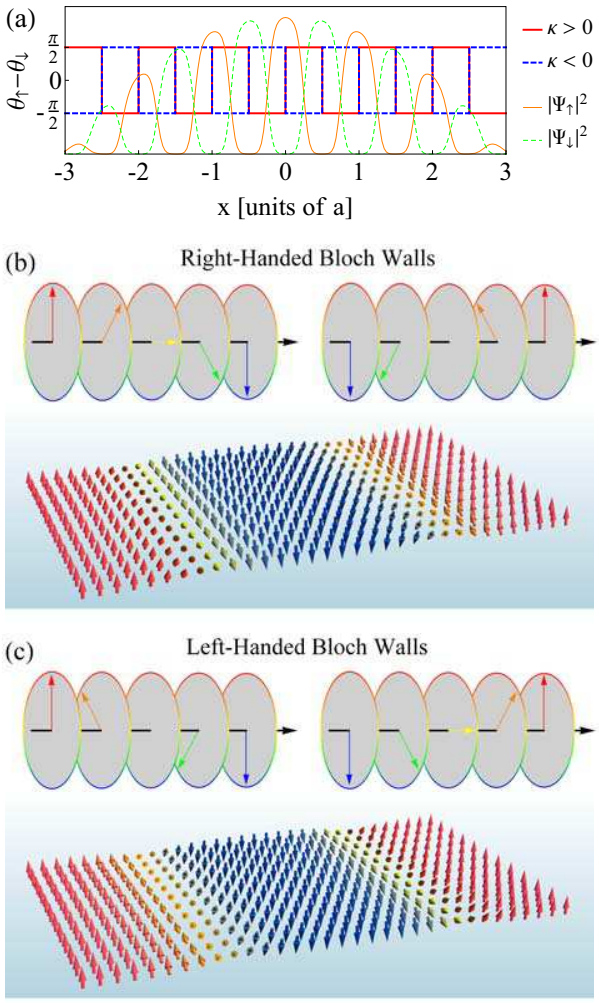

FIG. 5: (Color online) Domain wall chirality. (a) Section view of the relative phase $\theta_\uparrow - \theta_\downarrow$ along the x axis. The presence of Rashba SO coupling locks the relative phase at $\pm\pi/2$, and the periodic change of the densities along the x direction induces a periodic modulation of the relative phase between $\pi/2$ and $-\pi/2$. By tuning the sign of the Rashba SO coupling from positive ($\kappa > 0$) to negative ($\kappa < 0$), the relative phase will be changed from $\pm\pi/2$ (red thick line) to $\mp\pi/2$ (blue thick dashed line). (b) An illustration of right-handed chiral Bloch walls stabilized by positive Rashba SO coupling with $\kappa > 0$. (c) An illustration of left-handed chiral Bloch walls stabilized by negative Rashba SO coupling with $\kappa < 0$. By crossing a right-handed (left-handed) chiral Bloch wall, the spin vector flips like a right-rotating (left-rotating) spiral.

The relative phase plays an important role in determining the type of the domain walls, which separate the spin-up and spin-down domains [60]. From the definition of the spin density vector $\mathbf{S}$, one finds that S_z is uniquely determined by the relative density, while the direction of the spin projection on the S_x-S_y plane is determined by the relative phase and can be represented by an azimuthal angle $\alpha = \arctan(S_y/S_x) = \theta_\downarrow - \theta_\uparrow$. In the absence of SO coupling, the two component con-

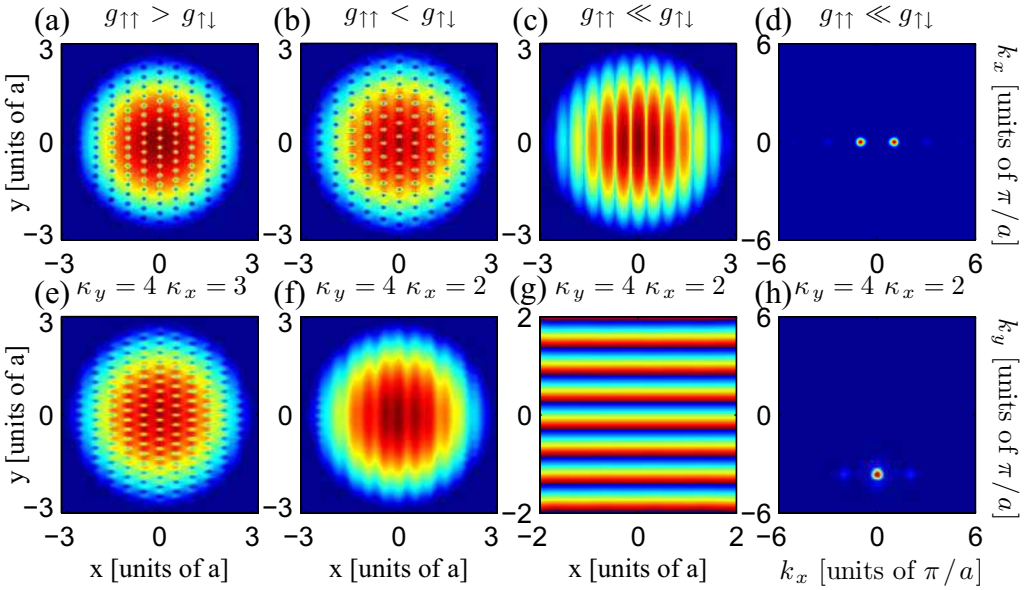
(a) $g_{\uparrow\uparrow} > g_{\uparrow\downarrow}$
(b) $g_{\uparrow\uparrow} < g_{\uparrow\downarrow}$
(c) $g_{\uparrow\uparrow} \ll g_{\uparrow\downarrow}$
(d) $g_{\uparrow\uparrow} \ll g_{\uparrow\downarrow}$
(e) $\kappa_y = 4\ \kappa_x = 3$
(f) $\kappa_y = 4\ \kappa_x = 2$
(g) $\kappa_y = 4\ \kappa_x = 2$
(h) $\kappa_y = 4\ \kappa_x = 2$
y [units of a]
x [units of a]
k_x [units of π/a]
k_y [units of π/a]

FIG. 6: (Color online) Effects of asymmetric interaction and anisotropic spin-orbit coupling. (a-c) Density distributions of Bose condensates with Rashba SO coupling and asymmetric interaction. While the intra-component interaction is fixed with $\tilde{g}_{\uparrow\uparrow} = \tilde{g}_{\downarrow\downarrow} = 6000$, the inter-component interactions are varied to be (a) $\tilde{g}_{\uparrow\downarrow} = 3000$, (b) $\tilde{g}_{\uparrow\downarrow} = 7000$, and (c) $\tilde{g}_{\uparrow\downarrow} = 18000$. The Rashba SO-coupling strength is taken as $\kappa = 4\pi\hbar/ma$ in these plots. Notice that a sufficiently strong inter-component interaction can drive the system from the supersolid phase to the superfluid phase. (e, f) Density distributions of Bose condensates in the presence of anisotropic SO interaction with $\kappa_x \neq \kappa_y$. Parameters used in these two plots are (e) $\kappa_x = 3\pi\hbar/ma$, $\kappa_y = 4\pi\hbar/ma$ and (f) $\kappa_x = 2\pi\hbar/ma$, $\kappa_y = 4\pi\hbar/ma$. Here, the interatomic interaction are considered to be SU(2) symmetric with $\tilde{g} = 6000$. By increasing the SO-coupling anisotropy beyond a certain value, the system will undergo a phase transition and become a superfluid which can be regarded as a plane-wave state characterized by phase modulation shown in (g). We emphasize that the superfluid phases driven by asymmetric interaction (c) and by anisotropic SO coupling (f) acquire different properties, as can be easily distinguished from the momentum distribution depicted in (d) and (h), respectively. In this figure, the periodic potential depth is taken as $V_0 = 20\pi^2\hbar^2/ma^2$.

densates have an arbitrary relative phase, such that the spin projection on the S_x-S_y plane within the domain wall can take arbitrary directions. In the presence of SO coupling, the relative phase is locked at $\pm\pi/2$, thus the spin rotational symmetry in the S_x-S_y plane is broken. As $S_x = 2|\Psi_\uparrow||\Psi_\downarrow|\cos(\theta_\uparrow - \theta_\downarrow)/(|\Psi_\uparrow|^2 + |\Psi_\downarrow|^2)$, obviously we have $S_x = 0$. This implies that the spins on the domain wall are confined within the S_y-S_z plane and form a Bloch wall, crossing which the spin vector rotates like a spiral [61].

One important feature of a domain wall is its chirality, which distinguishes the right-handed rotation from the left-handed rotation as moving between domains. Domain wall chirality has been recently investigated in ultrathin ferromagnetic films [61–63]. As a new controllable degree of freedom, domain wall chirality opens up new opportunities for spintronics device designs, and has potential application in information processing and storage. In the present system, we find that the chirality of the Bloch walls can be manipulated by changing the sign of the Rashba SO coupling. According to Eq. (2), if one changes the sign of the Rashba SO-coupling constant, the relative phase will jump between $\pm\pi/2$ [see Fig. 5(a)]. As $S_y = -2|\Psi_\uparrow||\Psi_\downarrow|\sin(\theta_\uparrow - \theta_\downarrow)/(|\Psi_\uparrow|^2 + |\Psi_\downarrow|^2)$, changing the sign of the relative phase will change the sign of S_y, and hence the chirality of the Bloch walls. Typical examples of the spin configurations are given in Figs. 5(b) and 5(c), where the right-handed and left-handed chiral Bloch walls correspond to positive and negative Rashba SO-coupling constants, respectively. In a realistic experiment, the sign of the Rashba SO coupling can be varied by tuning the phase of the rf field [53] in the proposal described in Appendix A.

V. EFFECTS OF ASYMMETRIC INTERACTION AND ANISOTROPIC SPIN-ORBIT COUPLING

In the discussion above, we have focused on the case of SU(2) symmetric interaction with $g_{\uparrow\uparrow} = g_{\downarrow\downarrow} = g_{\uparrow\downarrow}$. It is important to consider also the non-SU(2) symmetric interaction with $g_{\uparrow\uparrow} = g_{\downarrow\downarrow} \neq g_{\uparrow\downarrow}$. We find that if a supersolid phase can be stabilized with a proper combination of SO-coupling strength κ and periodic potential depth V_0 with a SU(2) symmetric interaction, an asymmetric interaction with $g_{\uparrow\uparrow} > g_{\uparrow\downarrow}$ always favors the supersolid phase, as shown in Fig. 6(a). The supersolid phase is also stable for $g_{\uparrow\uparrow} < g_{\uparrow\downarrow}$ provided that the difference in $g_{\uparrow\downarrow}$ and $g_{\uparrow\uparrow}$ is sufficiently small, $g_{\uparrow\downarrow} - g_{\uparrow\uparrow} \ll g_{\uparrow\downarrow}$. Such

a situation corresponds to Fig. 6(b). As one further increases the asymmetry such that $g_{\uparrow\uparrow} \ll g_{\uparrow\downarrow}$, the supersolid phase becomes unfavorable and is replaced by the superfluid phase [Figs. 6(c) and 6(d)].

Additionally we have also considered the anisotropy effects of the SO coupling. By decreasing κ_x we find that the supersolid phase, if it exists in the Rashba case, remains stable for a certain range of $\kappa_x < \kappa_y$, as shown in Fig. 6(e). By further increasing the anisotropy, the system undergoes a phase transition and becomes a superfluid, as shown in Fig. 6(f). This superfluid phase can be regarded as a plane-wave state characterized by a phase modulation in the y direction, as shown in Fig. 6(g). The momentum distribution for this case is illustrated in Fig. 6(h). In particular, when $\kappa_x = 0$, the SO coupling becomes unidirectional and reduces to that of the National Institute of Standards and Technology scheme [23–25], and the supersolid phase with nontrivial topological spin texture is no longer formed.

VI. DISCUSSION

The system considered can be realized experimentally in ^{87}Rb condensates using two magnetic states $|F = 1, m_F = 1\rangle$ and $|F = 1, m_F = -1\rangle$ of the $F = 1$ ground-state manifold. The Rashba SO coupling and spin-dependent periodic potential can be implemented by a combination of magnetic pulses [53, 54], and a pair of cross-linear polarized counterpropagating laser beams [50, 51]. The detail proposal is given in Appendix A. Considering a typical experimental situation in which a total of $N = 1.7 \times 10^5$ atoms with the s-wave scattering length $a_{\alpha\beta} \approx 100 a_B$ (a_B is the Bohr radius) are confined in a harmonic trap with the frequencies $\omega_\perp \approx 2\pi \times 40$ Hz and $\omega_z \approx 2\pi \times 200$ Hz, we obtain the effective interaction parameter $\tilde{g} \approx 6000$. By using a CO_2 laser operated at a wavelength of 10.6 μm, one can produce a lattice constant a coinciding with $\pi\sqrt{\hbar/m\omega_\perp}$. These are consistent with the parameters used in our calculations.

The supersolid phase can be identified either by a direct observation of the lattice structure via *in-situ* measurements [64, 65] or by momentum distribution measurements using the time-of-fight imaging technique [66]. The topological spin configurations of the meron-pair textures, as well as the chiral domain walls, can be imaged nondestructively with a high spatial resolution by the magnetization-sensitive phase-contrast imaging technique [67]. The domain wall chirality can also be determined by extracting the relative phase from the dual state imaging technique [68].

To summarize, we have studied the spin-orbit-coupled Bose-Einstein condensates in a spin-dependent periodic potential. We have demonstrated that the interplay between the spin-orbit coupling and the spin-dependent periodic potential leads to the emergence of a supersolid phase, which features a concomitant magnetic ordering with topologically nontrivial spin textures. We have explored the phase diagram of the system upon changing the spin-orbit-coupling strength and the periodic potential depth, and investigated the effects of asymmetric interatomic interaction and anisotropic spin-orbit coupling. Proposals to realize and observe the supersolid phase within realistic experimental situations have also been discussed.

ACKNOWLEDGMENTS

This work was supported by the NKBRSFC under Grants No. 2011CB921502 and No. 2012CB821305; NSFC under Grants No. 61227902, No. 61378017, No. 11274009, and No. 11375030; SPRPCAS under Grant No. XDB01020300; and the European Social Fund under the Global Grant measure.

APPENDIX A: CREATING SPIN-ORBIT-COUPLED BOSE GASES IN A SPIN-DEPENDENT PERIODIC POTENTIAL

We consider a two-component Bose gas of ultacold alkali atoms, such as ^{87}Rb, with two internal states chosen to be the hyperfine states $|F = 1, m_F = 1\rangle$ and $|F = 1, m_F = -1\rangle$ of the $F = 1$ ground-state manifold. The protocol for implementing the spin-orbit (SO) coupling and the spin-dependent periodic potential is illustrated in Fig. 7. It relies on the ability to switch between magnetic pulses and laser pulses [see Fig. 7(b)].

The first two stages of the scheme represent a modified version of a recent proposal [53] to produce SO coupling by means of magnetic pulses. Originally it was proposed to create the SO coupling using a strong time-independent bias magnetic field along the quantization axis z and infrared (IR) magnetic field in the x-y plane with a frequency ω in resonance with splitting between the magnetic sublevels induced by the bias field [53]. Yet now we are dealing with the hyperfine states $|F = 1, m_F = 1\rangle$ and $|F = 1, m_F = -1\rangle$, which cannot be directly coupled by such magnetic pulses. To bypass the problem, we propose to use simultaneously two IR magnetic fields in the x-y plane with different frequencies $\omega_1 \neq \omega_2$, where frequency sum $\omega_1 + \omega_2$ is equal to the magnetic splitting between the two sublevels. This provides a two photon coupling between the hyperfine states $|F = 1, m_F = 1\rangle$ and $|F = 1, m_F = -1\rangle$. The corresponding second-order coupling Hamiltonian can be made proportional to σ_x or σ_y depending on the phases of the IR fields, like in Ref. [53], where σ_x and σ_y are the quasi-spin operators for the selected pair of states.

The magnetic field $\mathbf{B}_1$ with frequency ω_1 is taken to be uniform and oriented along the x axis. Another magnetic field $\mathbf{B}_2$ with frequency ω_2 is produced by a pair of wires along the y or x axis for the first ($0 \leq t < \tau$) and the second ($\tau \leq t < 2\tau$) stages, respectively [53]. By going to the rotating frame to eliminate the bias field along the z

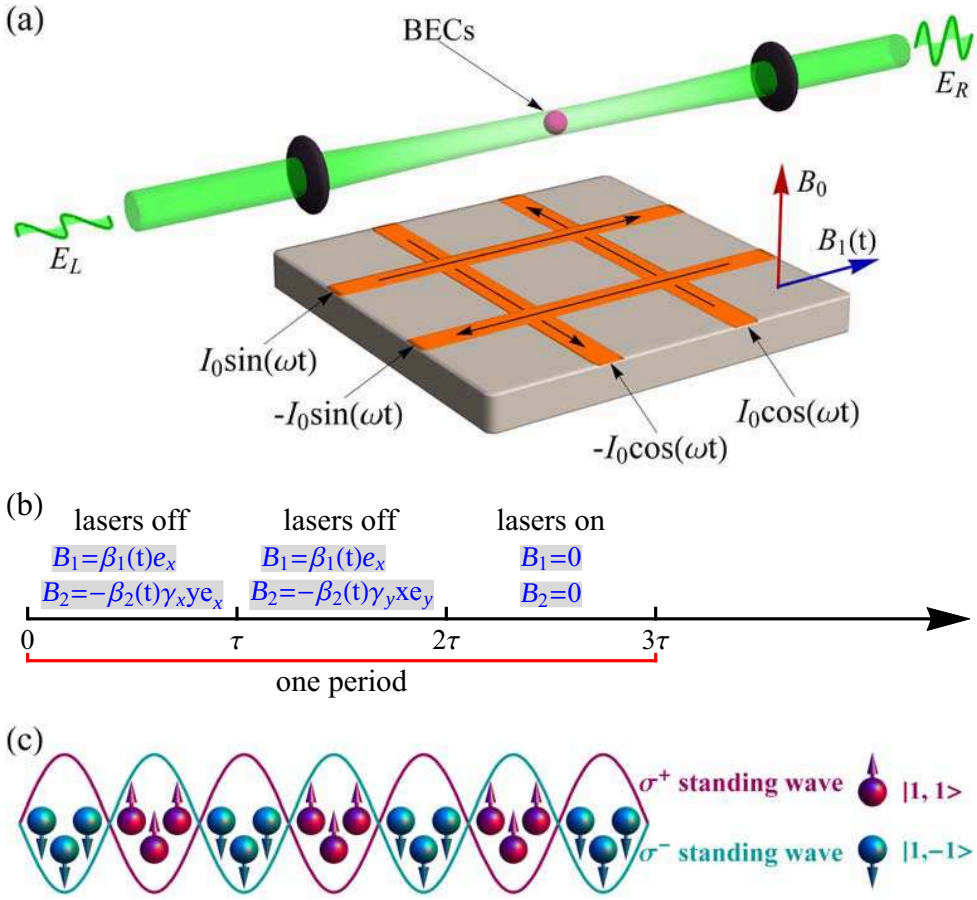

FIG. 7: (Color online) Experimental setup for creating spin-orbit-coupled Bose gases in a spin-dependent periodic potential. (a) The cloud of atoms is situated tens of micrometers above the surface of an atom chip. Two pairs of parallel microwires with amplitude modulated rf current are embedded in the chip, and produce periodic pulsed magnetic field gradients along perpendicular directions. Another pulsed uniform magnetic field oriented along the x axis is added, with the sum frequency of the two magnetic fields equal to the magnetic splitting induced by a strong bias field $B_0\mathbf{e}_z$ between the sublevels $m_F = \pm 1$. This provides a two-photon coupling between the hyperfine states, and induces an effective 2D SO coupling in the first-order approximation to the pulse duration τ. Two counterpropagating linearly polarized laser beams with the same frequency but perpendicular polarization vectors create a spin-dependent periodic potential. (b) The pulse sequence used to implement SO coupling and spin-dependent periodic potential. The parameters γ_x and γ_y characterize the strength of the magnetic field gradient, and $\beta_1(t)$ and $\beta_2(t)$ define the temporal shape of the magnetic fields. (c) Two polarized standing wave laser fields σ^+ (purple) and σ^- (cyan) are produced by the counterpropagating linearly polarized lasers in (a). Due to the polarization-dependent a.c. Stark shift, the internal state $|1,1\rangle$ is affected by the standing wave laser field σ^+, while the internal state $|1,-1\rangle$ experiences the standing wave laser field σ^-.

direction, choosing the proper phases of the IR magnetic fields, and making the rotating-wave-approximation to neglect the fast oscillating terms, the second order coupling induced by the IR fields can yield the SO-coupling terms $-i\hbar\kappa_x\sigma_x\partial_x$ and $-i\hbar\kappa_y\sigma_y\partial_y$ for the first and second stages respectively. The SO-coupling parameters κ_x and κ_y depend on the strength of the magnetic pulses and the detuning from the single photon resonance, and also require some quadratic Zeeman shift in order to be non-zero [69]. The first two stages provide a 2D SO coupling [53, 54] $\mathcal{V}_{\rm so} = -i\hbar(\kappa_x\sigma_x\partial_x + \kappa_y\sigma_y\partial_y)$ in the first-order approximation, which is valid for a sufficiently short duration τ. In particular, for $\kappa_x = \kappa_y$, one arrives at the isotropic Rashba-type SO coupling.

In the third stage, $2\tau \le t < 3\tau$, the magnetic field is turned off, and two counterpropagating laser beams are applied with the same frequency but perpendicular linear polarization vectors [see Fig. 7(a)]. In this case, a standing wave light field is formed. It can be decomposed into a superposition of σ^+ and σ^- polarized standing waves, giving rise to periodic potentials $V_+ = V_0\sin^2(\pi x/a)$ and $V_- = V_0\cos^2(\pi x/a)$ [51]. Due to the polarization-dependent a.c. Stark shift, atoms in different hyperfine states will feel significantly different potentials [70]. For the $F = 1$ ground-state manifold chosen above, the internal state $|F = 1, m_F = 1\rangle$ experiences the V_+ potential and the internal state $|F = 1, m_F = -1\rangle$ is affected by the V_- potential. This leads to the formation of the spin-

dependent periodic potential [71], as shown in Fig. 7(c).

APPENDIX B: CALCULATING THE MANY-BODY GROUND STATES

We investigate the many-body effects based on the Gross-Pitaevskii mean-field theory. It is well expected that a mean-field approach is valid provided that the system is far away from a quantum critical point such that the quantum fluctuation effects are not significant. In the case of one-dimensional optical lattice where each lattice site is essentially a one-dimensional tube containing a large number of particles, the Wannier function can be drastically altered from the single-particle form by the interaction effect. As a consequence, the critical value of lattice depth is dependent on the atom number on each lattice site [72]. For the parameters considered in this manuscript, the particle number in each tube is as high as several thousand, which ensures that the critical value of lattice depth is above 90 recoil energy. Thus, we expect the mean-field approach to give a satisfactory description of the system for $V_0 \lesssim 90$ recoils.

The validity of the Gross-Pitaevskii mean-field approximation used above can be checked by evaluating the quantum depletion caused by quantum fluctuations [55]. According to the Bogoliubov theory, the fluctuation part $\delta\hat{\Psi}_\alpha(\mathbf{r},t)$ around the condensate can be subjected to a canonical transformation resulting in the expansion $\delta\hat{\Psi}_\alpha(\mathbf{r},t) = \sum_j \left[u_{\alpha j}(\mathbf{r})e^{-i\omega_j t}\hat{\gamma}_j + v^*_{\alpha j}(\mathbf{r})e^{i\omega_j t}\hat{\gamma}^\dagger_j\right]$, where $\hat{\gamma}_j$ and $\hat{\gamma}^\dagger_j$ are the quasiparticle creation and annihilation operators associated with the jth collective mode. The mode functions $u_{\alpha i}(\mathbf{r})$, $v_{\alpha i}(\mathbf{r})$ and collective frequencies ω_j are determined by the Bogoliubov-de Gennes (BdG) equations

$$\begin{bmatrix} H_{s_\uparrow}+g_{\uparrow\uparrow}|\Psi_\uparrow|^2 & V_{\rm so}+g_{\uparrow\downarrow}\Psi_\uparrow\Psi^*_\downarrow & g_{\uparrow\uparrow}\Psi^2_\uparrow & g_{\uparrow\downarrow}\Psi_\uparrow\Psi_\downarrow \\ -V^*_{\rm so}+g_{\downarrow\uparrow}\Psi_\downarrow\Psi^*_\uparrow & H_{s_\downarrow}+g_{\downarrow\downarrow}|\Psi_\downarrow|^2 & g_{\downarrow\uparrow}\Psi_\downarrow\Psi_\uparrow & g_{\downarrow\downarrow}\Psi^2_\downarrow \\ g_{\uparrow\uparrow}\Psi^{*2}_\uparrow & g_{\uparrow\downarrow}\Psi^*_\uparrow\Psi^*_\downarrow & H_{s_\uparrow}+g_{\uparrow\uparrow}|\Psi_\uparrow|^2 & V^*_{\rm so}+g_{\uparrow\downarrow}\Psi^*_\uparrow\Psi_\downarrow \\ g_{\downarrow\uparrow}\Psi^*_\downarrow\Psi^*_\uparrow & g_{\downarrow\downarrow}\Psi^{*2}_\downarrow & -V_{\rm so}+g_{\downarrow\uparrow}\Psi^*_\downarrow\Psi_\uparrow & H_{s_\downarrow}+g_{\downarrow\downarrow}|\Psi_\downarrow|^2 \end{bmatrix} \begin{bmatrix} u_{\uparrow i}(\mathbf{r}) \\ u_{\downarrow i}(\mathbf{r}) \\ v_{\uparrow i}(\mathbf{r}) \\ v_{\downarrow i}(\mathbf{r}) \end{bmatrix} = \hbar\omega_i \begin{bmatrix} u_{\uparrow i}(\mathbf{r}) \\ u_{\downarrow i}(\mathbf{r}) \\ -v_{\uparrow i}(\mathbf{r}) \\ -v_{\downarrow i}(\mathbf{r}) \end{bmatrix}, \tag{B1}$$

under the normalization $\int \left(|u_{\uparrow i}|^2 + |u_{\downarrow i}|^2 - |v_{\uparrow i}|^2 - |v_{\downarrow i}|^2\right)d\mathbf{r} = 1$. Here, $H_{s_\uparrow} = H_{\rm osc} + V_\uparrow + g_{\uparrow\uparrow}|\Psi_\uparrow|^2 + g_{\uparrow\downarrow}|\Psi_\downarrow|^2 - \mu$, $H_{s_\downarrow} = H_{\rm osc} + V_\downarrow + g_{\downarrow\downarrow}|\Psi_\downarrow|^2 + g_{\downarrow\uparrow}|\Psi_\uparrow|^2 - \mu$ with $H_{\rm osc} = -\frac{\hbar^2}{2m}\nabla^2 + V_{\rm H}$ and μ the chemical potential, and $V_{\rm so} = -\hbar(i\kappa_x\partial_x + \kappa_y\partial_y)$. At zero temperature, the number of the non-condensate particles can be calculated by $\delta N = \int\sum_j \left(|v_{\uparrow i}|^2 + |v_{\downarrow i}|^2\right)d\mathbf{r}$, where j is restricted by the nonnegative mode frequencies $\omega_j > 0$.

By numerically solving the BdG equations (B1) in two dimension, we find that the quantum depletion is small not only in the superfluid phase but also in the supersolid phase, thus the quantum fluctuations can be neglected. In Figs. 8(a) and 8(b), we present the quantum depletion $\delta N/(N+\delta N)$ as a function of the SO-coupling strength κ and the periodic potential depth V_0, respectively. One can see that, the quantum depletion is always less than 0.1%, thereby confirming the validity of the Gross-Pitaevskii approach.

By numerically minimizing the energy functional, we can obtain the many-body ground-state wave functions. A valid and widely used method for the minimization is the imaginary time algorithm [73, 74]. In solving the imaginary time evolution equations, we develop a backward-forward Euler Fourier-pseudospectral (BFFP) discretization. For the time discretization, we use the backward or forward Euler scheme for linear or nonlinear terms in time derivatives. For the spatial discretization, we take fast Fourier transform (FFT) in spatial derivatives. A similar discretization scheme, named backward-forward Euler sine-pseudospectral (BFSP) discretization, has been proposed and demonstrated for Bose systems without SO coupling [75].

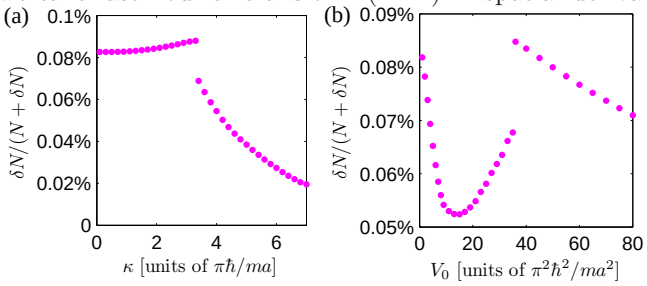

FIG. 8: (Color online) Quantum depletion as a function of the spin-orbit-coupling strength (a) and the periodic potential depth (b). The periodic potential depth is fixed at $V_0 = 20\pi^2\hbar^2/ma^2$ in (a), and the spin-orbit-coupling strength is fixed at $\kappa = 4\pi\hbar/ma$ in (b). The dimensionless interaction parameter is taken as $\tilde{g} = 6000$. The quantum depletion is always less than 0.1%, thereby confirming the validity of the mean-field approach.

[1] A. F. Andreev and I. M. Lifshitz, Sov. Phys. JETP **29**, 1107 (1969).
[2] G. V. Chester, Phys. Rev. A **2**, 256 (1970).
[3] A. J. Leggett, Phys. Rev. Lett. **25**, 1543 (1970).
[4] M. W. Meisel, Physica B **178**, 121 (1992).
[5] S. Balibar and F. Caupin, J. Phys.: Condens. Matter **20**, 173201 (2008).
[6] M. Boninsegni and N. V. Prokof'ev, Rev. Mod. Phys. **84**, 759 (2012).
[7] S. Balibar, Nature (London) **464**, 176 (2010).
[8] E. Kim and M. H. W. Chan, Nature (London) **427**, 225 (2004).
[9] J. Ye, Phys. Rev. Lett. **97**, 125302 (2006).
[10] J. Day and J. Beamish, Nature (London) **450**, 853 (2007).
[11] B. Hunt, E. Pratt, V. Gadagkar, M. Yamashita, A. V. Balatsky, and J. C. Davis, Science **324**, 632 (2009).
[12] H. Choi, D. Takahashi, K. Kono, and E. Kim, Science **330**, 1512 (2010).
[13] D. Y. Kim and M. H. W. Chan, Phys. Rev. Lett. **109**, 155301 (2012).
[14] N. Henkel, R. Nath, and T. Pohl, Phys. Rev. Lett. **104**, 195302 (2010).
[15] F. Cinti, P. Jain, M. Boninsegni, A. Micheli, P. Zoller, and G. Pupillo, Phys. Rev. Lett. **105**, 135301 (2010).
[16] N. Henkel, F. Cinti, P. Jain, G. Pupillo, and T. Pohl, Phys. Rev. Lett. **108**, 265301 (2012).
[17] S. Wessel and M. Troyer, Phys. Rev. Lett. **95**, 127205 (2005).
[18] I. Danshita and C. A. R. Sá de Melo, Phys. Rev. Lett. **103**, 225301 (2009).
[19] O. Tieleman, A. Lazarides, and C. Morais Smith, Phys. Rev. A **83**, 013627 (2011).
[20] M. Boninsegni, J. Low. Temp. Phys. **168**, 137 (2012).
[21] M. Lewenstein, A. Sanpera, V. Ahufinger, B. Damski, A. Sen(De), and U. Sen, Adv. Phys. **56**, 243 (2007).
[22] I. Bloch, J. Dalibard, and W. Zwerger, Rev. Mod. Phys. **80**, 885 (2008).
[23] Y. J. Lin, K. Jiménez-García, and I. B. Spielman, Nature (London) **471**, 83 (2011).
[24] J. Y. Zhang, S. C. Ji, Z. Chen, L. Zhang, Z. D. Du, B. Yan, G. S. Pan, B. Zhao, Y. J. Deng, H. Zhai, S. Chen, and J. W. Pan, Phys. Rev. Lett. **109**, 115301 (2012).
[25] S. C. Ji, J. Y. Zhang, L. Zhang, Z. D. Du, W. Zheng, Y. J. Deng, H. Zhai, S. Chen, and J. W. Pan, Nat. Phys. **10**, 314 (2014).
[26] P. Wang, Z. Q. Yu, Z. Fu, J. Miao, L. Huang, S. Chai, H. Zhai, and J. Zhang, Phys. Rev. Lett. **109**, 095301 (2012).
[27] L. W. Cheuk, A. T. Sommer, Z. Hadzibabic, T. Yefsah, W. S. Bakr, and M. W. Zwierlein, Phys. Rev. Lett. **109**, 095302 (2012).
[28] C. Qu, C. Hamner, M. Gong, C. Zhang, and P. Engels, Phys. Rev. A **88**, 021604(R) (2013).
[29] Z. Fu, L. Huang, Z. Meng, P. Wang, L. Zhang, S. Zhang, H. Zhai, P. Zhang, and J. Zhang, Nat. Phys. **10**, 110 (2014).
[30] J. Dalibard, F. Gerbier, G. Juzeliūnas, and P. Öhberg, Rev. Mod. Phys. **83**, 1523 (2011).
[31] V. Galitski and I. B. Spielman, Nature (London) **494**, 49 (2013).
[32] X. Zhou, Y. Li, Z. Cai, and C. Wu, J. Phys. B **46**, 134001 (2013).
[33] A. M. Dudarev, R. B. Diener, I. Carusotto, and Q. Niu, Phys. Rev. Lett. **92**, 153005 (2004).
[34] T. D. Stanescu, B. Anderson, and V. Galitski, Phys. Rev. A **78**, 023616 (2008).
[35] C. Wu, I. Mondragon-Shem, and X. F. Zhou, Chin. Phys. Lett. **28**, 097102 (2011).
[36] R. Liao, Y. Yi-Xiang, and W. M. Liu, Phys. Rev. Lett. **108**, 080406 (2012).
[37] W. S. Cole, S. Zhang, A. Paramekanti, and N. Trivedi, Phys. Rev. Lett. **109**, 085302 (2012).
[38] W. Zhang and W. Yi, Nat. Commun. **4**, 2711 (2013).
[39] C. Wang, C. Gao, C. M. Jian, and H. Zhai, Phys. Rev. Lett. **105**, 160403 (2010).
[40] T. L. Ho and S. Zhang, Phys. Rev. Lett. **107**, 150403 (2011).
[41] H. Sakaguchi, B. Li, and B. A. Malomed, Phys. Rev. E **89**, 032920 (2014).
[42] Z. F. Xu, R. Lü, and L. You, Phys. Rev. A **83**, 053602 (2011).
[43] H. Hu, B. Ramachandhran, H. Pu, and X. J. Liu, Phys. Rev. Lett. **108**, 010402 (2012).
[44] S. Sinha, R. Nath, and L. Santos, Phys. Rev. Lett. **107**, 270401 (2011).
[45] S. W. Su, I. K. Liu, Y. C. Tsai, W. M. Liu, and S. C. Gou, Phys. Rev. A **86**, 023601 (2012).
[46] Y. Deng, J. Cheng, H. Jing, C. P. Sun, and S. Yi, Phys. Rev. Lett. **108**, 125301 (2012).
[47] S. Gopalakrishnan, I. Martin, and E. A. Demler, Phys. Rev. Lett. **111**, 185304 (2013).
[48] Y. Chen, J. Ye, and G. Tian, J. Low. Temp. Phys. **169**, 149 (2012).
[49] Y. Li, G. I. Martone, L. P. Pitaevskii, and S. Stringari, Phys. Rev. Lett. **110**, 235302 (2013).
[50] I. H. Deutsch and P. S. Jessen, Phys. Rev. A **57**, 1972 (1998).
[51] O. Mandel, M. Greiner, A. Widera, T. Rom, T. W. Hänsch, and I. Bloch, Phys. Rev. Lett. **91**, 010407 (2003).
[52] N. Goldman, G. Juzeliūnas, P. Öhberg, and I. B. Spielman, Rep. Prog. Phys. **77**, 126401 (2014).
[53] B. M. Anderson, I. B. Spielman, and G. Juzeliūnas, Phys. Rev. Lett. **111**, 125301 (2013).
[54] Z. F. Xu, L. You, and M. Ueda, Phys. Rev. A **87**, 063634 (2013).
[55] C. J. Pethick and H. Smith, *Bose-Einstein Condensation in Dilute Gases* (Cambridge University Press, Cambridge, 2002).
[56] G. E. Volovik, *The Universe in a Helium Droplet* (Oxford University Press, New York, 2003).
[57] K. Kasamatsu, M. Tsubota, and M. Ueda, Phys. Rev. Lett. **93**, 250406 (2004).
[58] V. Schweikhard, I. Coddington, P. Engels, S. Tung, and E. A. Cornell, Phys. Rev. Lett. **93**, 210403 (2004).
[59] S. W. Su, C. H. Hsueh, I. K. Liu, T. L. Horng, Y. C. Tsai, S. C. Gou, and W. M. Liu, Phys. Rev. A **84**, 023601 (2011).
[60] B. A. Malomed, H. E. Nistazakis, D. J. Frantzeskakis, and P. G. Kevrekidis, Phys. Rev. A **70**, 043616 (2004).
[61] G. Chen, T. Ma, A. T. N'Diaye, H. Kwon, C. Won, Y. Wu, and A. K. Schmid, Nat. Commun. **4**, 2671 (2013).
[62] K. S. Ryu, L. Thomas, S. H. Yang, and S. Parkin, Nat.

Nanotechnol. **8**, 527 (2013).
[63] S. Emori, U. Bauer, S. M. Ahn, E. Martinez, and G. S. D. Beach, Nat. Mater. **12**, 611 (2013).
[64] N. Gemelke, X. Zhang, C. L. Hung, and C. Chin, Nature (London) **460**, 995 (2009).
[65] W. S. Bakr, A. Peng, M. E. Tai, R. Ma, J. Simon, J. I. Gillen, S. Fölling, L. Pollet, and M. Greiner, Science **329**, 547 (2010).
[66] P. T. Ernst, S. Götze, J. S. Krauser, K. Pyka, D. S. Lühmann, D. Pfannkuche, and K. Sengstock, Nat. Phys. **6**, 56 (2010).
[67] L. E. Sadler, J. M. Higbie, S. R. Leslie, M. Vengalattore, and D. M. Stamper-Kurn, Nature (London) **443**, 312 (2006).
[68] R. P. Anderson, C. Ticknor, A. I. Sidorov, and B. V. Hall, Phys. Rev. A **80**, 023603 (2009).
[69] In the absence of the quadratic Zeeman shift, the two-photon transitions induced first by magnetic field $\mathbf{B}_1$ followed by $\mathbf{B}_2$ interfere destructively with the transitions induced by the magnetic fields in the opposite order: $\mathbf{B}_2$ followed by $\mathbf{B}_1$.
[70] R. Grimm, M. Weidemüller, and Y. B. Ovchinnikov, Adv. At., Mol., Opt. Phys. **42**, 95 (2000).
[71] D. McKay and B. DeMarco, New J. Phys. **12**, 055013 (2010).
[72] J. Li, Y. Yu, A. M. Dudarev, and Q. Niu, New J. Phys. **8**, 154 (2006).
[73] F. Dalfovo and S. Stringari, Phys. Rev. A **53**, 2477 (1996).
[74] M. L. Chiofalo, S. Succi, and M. P. Tosi, Phys. Rev. E **62**, 7438 (2000).
[75] W. Bao, I. L. Chern, and F. Y. Lim, J. Comput. Phys. **219**, 836 (2006).